

Magnetometry with Nitrogen-Vacancy Centers in Diamond

Kasper Jensen, Pauli Kehayias and Dmitry Budker

Abstract This chapter covers magnetic sensing with nitrogen-vacancy (NV) defect centers in diamond. The NV center fundamentals are introduced and NV optically detected magnetic resonance techniques for dc and ac magnetic sensing are summarized. After reviewing some successful sensing applications, the advantages for using NV magnetometry, as well as some ongoing challenges, are enumerated.

1 Introduction

Magnetometers made with nitrogen-vacancy (NV) color centers in diamond are a recent addition to our collection of magnetometry tools. They are useful for magnetometry with high spatial resolution, are technically quite simple to use, work well in ambient conditions, and are a new system with many avenues for improvements and applications. These features have propelled much of the recent burst in NV magnetometer development in recent years, while ongoing work aims to extend the best achievable sensitivity and scope of their utility. This chapter provides an overview (including references to representative work) of NV basic

K. Jensen (✉)
Niels Bohr Institute, University of Copenhagen, Blegdamsvej 17,
2100 Copenhagen Ø, Denmark
e-mail: kjensen@nbi.dk

D. Budker
Department of Physics, University of California, Berkeley, CA 94720, USA
e-mail: dbudker@gmail.com

P. Kehayias
Harvard-Smithsonian Center for Astrophysics, Cambridge, MA 02138, USA
e-mail: pauli.kehayias@cfa.harvard.edu

D. Budker
Helmholtz-Institute Mainz, Johannes Gutenberg University, Mainz, Germany

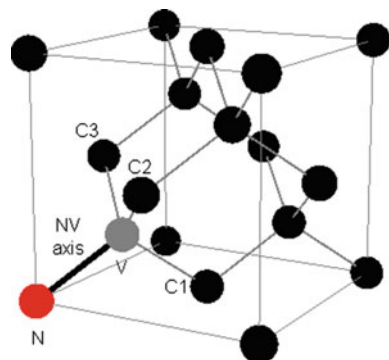
properties, magnetic sensing techniques, applications, and how NV centers fit into the broader scope of magnetometer technologies [1–4].

2 Physics of the NV Center

The NV center is a point defect in the diamond crystal lattice. It consists of a substitutional nitrogen atom and a neighboring vacancy, i.e. a missing carbon atom (Fig. 1). NV centers can have negative (NV^-), positive (NV^+), and neutral (NV^0) charge states, but NV^- is used for magnetometry and other applications. The NV^- center has six electrons. Five of the electrons are contributed from the dangling bonds of the three neighboring carbon atoms and the nitrogen atom. One extra electron is captured from an electron donor and gives rise to the negative charge state. The axis defined by the line connecting the nitrogen atom and the vacancy is called the NV axis. There are four possible ways that the nitrogen atom can be positioned with respect to the vacancy, leading to four possible NV alignments. The NV center has C_{3v} spatial point-group symmetry, i.e. its structure is symmetric with respect to rotations of 0 , $2\pi/3$ and $4\pi/3$ around the NV axis and to reflections in the mirror planes defined by the NV axis and one of the three neighboring carbon atoms. We can construct the energy levels of NV^- using a linear combinations of atomic orbitals (LCAO) group-theoretical approach [5, 6]. Figure 2 shows an energy-level diagram for NV electronic spin-triplet states (3A_2 and 3E) and electronic spin-singlet states (1E and 1A_1). The spin-triplet states each have three sub-levels with magnetic quantum number $m = 0, \pm 1$ where the quantization axis is set by the NV axis.

The optical transition between 3A_2 and 3E has a 637 nm wavelength (corresponding to red light) and the transition between 1E and 1A_1 has a 1042 nm wavelength (corresponding to infrared light). Both transitions have phonon sidebands due to vibrations in the diamond lattice. These phonon sideband transitions broaden the NV absorption and fluorescence spectra by hundreds of nanometers.

Fig. 1 Diamond crystal lattice with an NV center defect. The vacancy, nitrogen atom, and nearest-neighbor carbon atoms are labeled



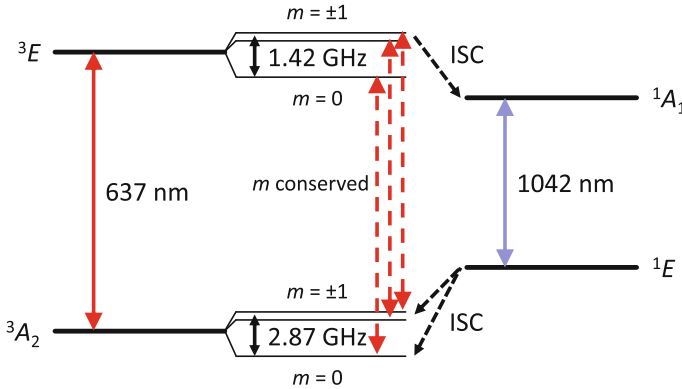


Fig. 2 NV electronic energy levels and optical transitions. The m -dependent intersystem crossing (ISC) from 3E enables optical initialization and readout

The ${}^3A_2 \rightarrow {}^3E$ transition can be excited with light with wavelength from ~ 450 to 637 nm, and one typically uses a 532 nm diode-pumped solid state laser to drive this transition. The fluorescence from the ${}^3E \rightarrow {}^3A_2$ decay is in the 637 to ~ 800 nm wavelength range. The optical transitions are largely spin-conserving, but there is also an intersystem crossing (ISC) between the spin-singlet and spin-triplet states. There is non-radiative decay from 3E to 1A_1 , and the ISC rate is higher for the $m = \pm 1$ states than for the $m = 0$ state [7, 8]. There is also a non-radiative ISC from 1E to 3A_2 .

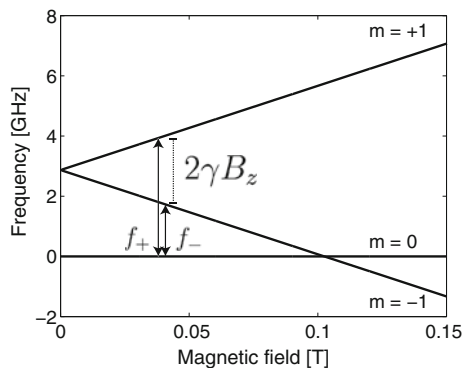
An important feature of the NV center is that it is possible to optically detect its spin state and optically pump it into the $m = 0$ sublevel. The mechanism for this is now described: assume the NV center is illuminated with resonant light that drives the ${}^3A_2 \rightarrow {}^3E$ transition. If the NV is initially in the ${}^3A_2, m = 0$ ground-state sublevel, it is excited to the ${}^3E, m = 0$ state as the optical transition is spin-conserving. The NV center decays back to the ${}^3A_2, m = 0$ sublevel, emitting fluorescence. This transition is cyclic and one detects a high fluorescence intensity when continuously illuminating the NV center. On the other hand, if the NV is initially in one of the ${}^3A_2, m = \pm 1$ ground-state sublevels, it is excited to the ${}^3E, m = \pm 1$ states, which have a substantial probability to undergo ISC to the singlet states. From the 1A_1 state, the NV center first decays to the 1E state, which has a 200 ns lifetime at room temperature [9]. Subsequently the NV center undergoes ISC to the 3A_2 state. Probabilistically, the NV center ends up in the $m = 0$ cycling transition after several excitation cycles, after which we say that the NV center has been optically pumped to the $m = 0$ state. When initially in one of the ${}^3A_2, m = \pm 1$ sublevels, an NV center emits less fluorescence from the ${}^3E \rightarrow {}^3A_2$ transition as it decays (largely nonradiatively) through the singlet states. By measuring fluorescence, one can read out the NV spin state from its fluorescence intensity.

The spin-triplet 3A_2 ground state is of particular importance. This state has a zero-field-splitting $D \approx 2.87$ GHz between the $m = 0$ and the $m = \pm 1$ sublevels

due to electron spin-spin interaction. Magnetic fields couple to the NV center through the Zeeman effect, which is described by the Hamiltonian $\mathcal{H}_B = \gamma \mathbf{B} \cdot \mathbf{S}$ (in units of hertz). Here, \mathbf{S} is the dimensionless spin-projection operator for the NV electronic spin and $\gamma \approx 28.0$ GHz/T is the electron gyromagnetic ratio. If a magnetic field $\mathbf{B} = B_z \hat{z}$ is aligned along the NV axis here chosen as the z direction, the energies of the m -sublevels are $E(m) = Dm^2 + \gamma B_z m$ (Fig. 3). Note that the energies of the $m = \pm 1$ sublevels depend linearly on the magnetic field. NV magnetometry is based on optical detection of this energy shift. The energies of the magnetic resonance transitions $m = 0 \leftrightarrow \pm 1$ are $\Delta E = D \pm \gamma B_z$, which are shown in Fig. 3 in frequency units as f_{\pm} . More generally, the vector magnetic field can be determined from these resonance frequencies.

The NV center has hyperfine structure due to the nuclear spin of the nitrogen atom. Nitrogen has two stable isotopes, ^{14}N (99.6 % natural abundance) with nuclear spin 1 and ^{15}N (0.4 % natural abundance) with nuclear spin 1/2. The nuclear spin state contributes additional terms to the Hamiltonian, written here in units of hertz as $\mathcal{H}_I = PI_z^2 + \gamma_N \mathbf{B} \cdot \mathbf{I}$ and $\mathcal{H}_{\text{hf}} = A_{\parallel} S_z I_z + A_{\perp} (S_x I_x + S_y I_y)$, where \mathbf{I} is the dimensionless spin-projection operator for the nuclear spin. When considering an ^{14}N nucleus, $P \approx -4.95$ MHz is the quadrupole splitting, $\gamma_N \approx 3.077$ MHz/T is the nuclear gyromagnetic ratio, and $A_{\parallel} \approx -2.16$ MHz and $A_{\perp} \approx -2.7$ MHz are the parallel and perpendicular hyperfine coupling parameters, respectively [10–12]. The nuclear Zeeman term $\gamma_N \mathbf{B} \cdot \mathbf{I}$ is usually small and can often be neglected. Due to the hyperfine coupling with the ^{14}N nuclear spin, each of the magnetic resonances f_+ and f_- will split into three transitions which conserve m_I . The hyperfine splittings can be observed in magnetic resonance spectra if the resonance linewidth is narrower than the splitting [13].

Fig. 3 Energy-level diagram for an NV center as a function of magnetic field when the magnetic field is aligned along the NV axis. The $m = 0 \leftrightarrow +1$ and $m = 0 \leftrightarrow -1$ transition frequencies are written as f_+ and f_- , respectively



3 Diamond Materials

Although natural diamonds can contain NV centers and other defects [14], one usually uses synthetic diamonds in order to have a better understanding of what the samples contain and to have a controlled and reproducible manufacturing method. There are several types of NV experiments that require different samples:

- NV ensemble experiments, where one interrogates many NV centers in a sample. The NV centers could be located in a thin sheet in the diamond or they could be distributed over a larger volume (throughout the entire diamond).
- Single-NV experiments, which use a diamond sample with few defects. One selects a particular NV with which to make measurements.
- NV nanodiamond experiments, which use nanodiamonds containing one or many NV centers. The nanodiamonds can be attached to atomic force microscopy (AFM) cantilevers, trapped in optical dipole traps, or functionalized and put into living cells [15–17].

There are several ways to manufacture diamond samples to suit these experimental requirements:

- High-pressure high-temperature (HPHT) growth, which is similar to natural diamond formation and is done in an anvil press at 5 GPa and 1700 K. After a solvent metal dissolves the carbon in a source graphite block, the carbon precipitates onto a seed crystal, which then grows. This growth technique yields samples with ~ 100 ppm of nitrogen.
- Chemical vapor deposition (CVD), where diamond is grown layer-by-layer in a gaseous environment. CVD growth produces samples with fewer nitrogen impurities (roughly 1 ppb to 1 ppm).
- Explosives detonation, which produces nanodiamonds with high nitrogen and NV densities.

HPHT and CVD growth can yield a variety of diamond qualities, such as polycrystalline, monocrystalline, optical-grade (with minimal birefringence and absorption), and electronic-grade diamond (with minimal impurity concentration). With a given manufacturing technique, one has further control over how NV centers are formed:

- During HPHT and CVD growth, one can control the nitrogen concentration in the growth environment, though most embedded nitrogen atoms do not form NV centers. These samples can be used as-is (for instance, in a single-NV experiment), but they are often irradiated or implanted to improve the NV density.
- One can bombard diamond samples with electrons, protons, neutrons, N^+ , N_2^+ , C^+ , or other particles to create vacancies and implant nitrogen. Varying the energy and species of the accelerated particles can create a uniform or near-surface defect layer. After creating vacancies, the NV density is not much

improved as the N and V locations are uncorrelated, but annealing the diamond samples after irradiation increases the NV yield. Annealing temperatures range from 700 to 1200 °C for several hours.

- The NV centers in an ensemble are usually randomly aligned, with 1/4 aligned along each crystallographic axis. However, CVD growth along certain crystallographic directions can create NV centers with preferential alignment, resulting in NV centers with primarily one or two alignments [18]. This is useful for NV ensemble magnetometry, where one might select NV centers with one alignment for sensing while the others contribute to background fluorescence.
- Delta doping is another technique for creating a nitrogen-doped layer during CVD growth. Nitrogen gas is introduced during slow CVD growth to embed a thin nitrogen layer in an otherwise pure diamond. Followed by irradiation and annealing, this can yield an NV layer (usually near the surface). To form the doped layer, ^{15}N is often added to the diamond growth environment to distinguish the near-surface NV centers from the deeper (^{14}N) NV centers. Delta doping ensures that CVD samples have few NV centers except near the surface, where they are most useful for sensing external fields. One can also use delta doping to create NV layers with known relative separations [19, 20].
- Bulk diamond samples can be turned into nanodiamonds by ball milling or chemical etching [21, 22].
- Diamond samples can be chemically etched to make diamond nanostructures, including optical waveguides, resonators, photonic crystals, or atomic force microscope (AFM) cantilevers [15, 23, 24].

4 Microscopy

One frequently optically probes NV centers with confocal microscopy setups, which are also used to characterize samples in biology and materials science. As shown in Fig. 4, a pump laser beam (often from a 532 nm solid-state laser) reflects off a dichroic mirror (which selectively reflects short optical wavelengths but transmits long wavelengths), is focused through a lens or microscope objective, and illuminates the diamond containing NV centers. The fluorescence from the NV centers is collected through the same lens, then passes through the dichroic mirror and onto a photodetector. A pinhole is used to filter out fluorescence from regions in the sample which are out of focus. NV confocal microscopy is used in several contexts:

- One can focus the pump laser beam onto the diamond and query a diffraction-limited volume of NV centers by measuring the collected fluorescence intensity with a single-pixel photodiode. One can sweep the interrogated volume by using scanning galvanometer mirrors or a piezo-driven objective or sample mount to obtain a wide-field image one pixel at a time [25].

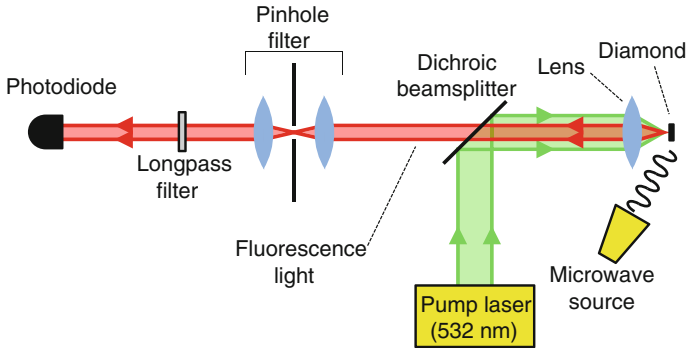


Fig. 4 A typical confocal microscopy setup for experiments with NV centers in diamond

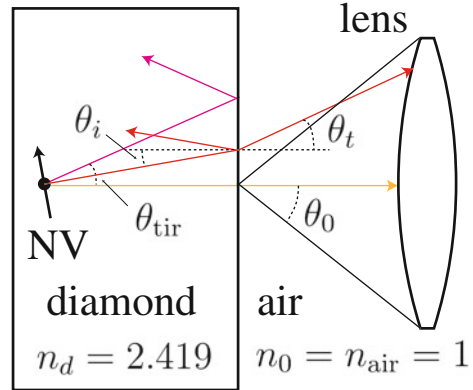
- Another option for wide-field imaging is to instead illuminate a wide area on the diamond and image the fluorescence with a camera. This enables diffraction-limited spatial resolution ($<1 \mu\text{m}$) for imaging individual NV centers or mapping the magnetic field over a spatial region [26]. This can be extended using sub-diffraction-limited imaging to few-nm resolution [27].
- One can use diamonds and NV centers in scanning-probe microscopy (such as AFM) and use optical readout to query the NV centers. This yields few-nm spatial resolution [15, 28]. A microscope objective collects fluorescence light from a diamond AFM probe containing an NV center, and moving the probe interrogates different spatial regions without significantly affecting the light collection. A diamond nanopillar probe can also enhance the light collection by directing fluorescence light to the objective.

While magnetometers based on NV centers in diamond are currently less sensitive than other technologies such as SQUID magnetometers and vapor cell magnetometers, the high spatial resolution is their main advantage. Confocal microscopy is quite universal in experiments with NV centers, though work is ongoing to overcome its primary sensitivity limitation which is photon shot noise (see Eq. 2) due to poor fluorescence collection efficiency [29–31].

5 Light Detection and Collection

Photon shot noise of the detected NV fluorescence often limits the magnetic field sensitivity. It is therefore important to detect NV fluorescence efficiently; however, one is only able to collect a fraction of the light emitted. This problem is quite severe, as the NV centers are inside the diamond host material which has a high index of refraction ($n_d \approx 2.419$). The first issue is that only part of the light exiting the diamond is collected by the microscope objective (or lens) in a confocal microscope. The collection efficiency depends on the numerical aperture NA of the

Fig. 5 NV fluorescence refraction and reflection at a diamond-air interface



objective, which is defined as $NA = n_0 \sin(\theta_0)$, where θ_0 is the maximum half-angle from which the objective can collect light and n_0 is the index of refraction outside the diamond (Fig. 5). For a given NA , light is collected within the angle $\theta_0 = \arcsin(NA/n_0)$. The numerical aperture typically ranges from 0.1 to 1 for air objectives and up to ~ 1.52 for oil-immersion objectives. The upper limit for NA is given by the index of refraction of either the air ($n_{air} \approx 1$) or the oil ($n_{oil} \approx 1.52$). There is also fluorescence refraction inside the diamond at the diamond interface. By Snell's law [$n_d \sin(\theta_i) = n_0 \sin(\theta_t)$], only light emitted within the angle $\theta_i^{\max} = \arcsin(NA/n_d)$ can exit the diamond and be collected by the objective. The maximum emission angles are $\theta_i^{\max} \approx 24^\circ$ and 39° for the best air ($NA = 1$) and oil-immersion objectives ($NA = 1.52$).

The second issue is that there are reflections of the emitted light from the diamond surface. As an example, for normal incidence the reflectance is $R = |(n_d - n_0)/(n_d + n_0)|^2$ using the Fresnel equations, which yields $R \approx 17\%$ at a diamond-air interface and $R \approx 5\%$ at a diamond-oil interface. As mentioned above, there is also total internal reflection at the diamond surface when $\theta_i \geq \theta_{tir} = \arcsin(n_0/n_d)$. The total collection efficiency of the light emitted from an NV center can be calculated taking the emission pattern of the NV center dipole into account (since the reflectance depends on the light polarization). The maximum collection efficiency is 4 or 10 % using either air (up to $NA = 1$) or oil-immersion objectives (up to $NA = 1.52$) [29].

There are several strategies for improving light collection efficiency. In Ref. [29] it was realized that when NV centers are excited from the top of a diamond plate, most of the fluorescent light undergoes multiple total internal reflections before it leaves the diamond plate at the sides perpendicular to the top. By placing photodiodes close to the four sides, a total of 47 % of the emitted fluorescence was collected. Other schemes use a solid-immersion lens (SIL), including lenses made from diamond [32, 33]. With this geometry, light emitted in the center of the SIL will not undergo refraction at the diamond-air interface as the light rays are perpendicular to the surface, improving the collection efficiency. Nanofabricated

diamond waveguides can also direct the emitted fluorescence out of the diamond, also improving the collection efficiency [23].

The fluorescence collection problem can be circumvented by instead detecting absorption of a probe laser beam. So far, schemes based on absorption of 637 nm red light and 1042 nm infrared (IR) light (see transitions in Fig. 2) have been demonstrated [34–37]. Red and infrared probe light can have spin-state-dependent absorption, a fact we can use to measure the 3A_2 magnetic resonance frequencies. When detecting the NV centers using infrared absorption one can in principle have an arbitrarily large photon flux without causing extra decoherence to the NV centers, thereby reducing the photon shot noise limitation to the magnetometer sensitivity (see Eq. 2). The amount of IR absorption depends on the $^1E \rightarrow ^1A_1$ sun cross-section, the NV density, and the thickness of the diamond. The first IR magnetometry experiment [35] was done at cryogenic temperatures ($T \approx 75$ K), where the absorption cross section is larger than at room temperature [38]. A later experiment employed an external optical cavity, enhancing the absorption by two orders of magnitude and enabling room-temperature operation of the magnetometer [37].

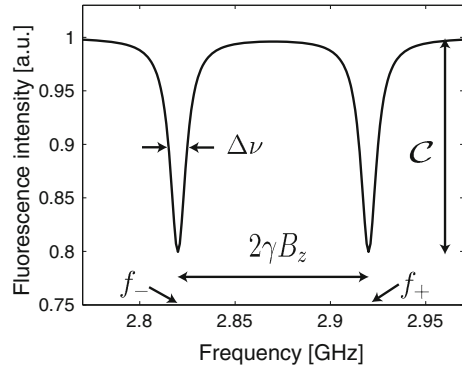
Another detection scheme is based on ionizing the NV^- to NV^0 conditionally on the NV^- 3A_2 sublevel, then reading out the charge state using a 594 nm probe laser [30]. Since NV^- fluoresces when illuminated with 594 nm light while NV^0 does not, this spin-to-charge-state readout scheme has high contrast with many readout photons. Yet another approach is to detect spin-state dependent photocurrent, making photon collection unnecessary [39]. Finally, cryogenic single-NV experiments can use a high-contrast optical readout technique that probes different $^3A_2 \rightarrow ^3E$ transitions [31].

6 Optically Detected Magnetic Resonance

Many of the techniques for NV magnetometry require a bias magnetic field of a certain amplitude and direction. Such static magnetic fields can be measured with the following continuous wave (CW) optically detected magnetic resonance (ODMR) technique.

Consider the typical confocal microscopy setup shown in Fig. 4 where 532 nm green light continuously illuminates the diamond sample. For simplicity, assume that the sample contains a single NV center within the confocal volume. The NV center is optically pumped into the $m = 0$ sublevel by the green light, and a high level of fluorescence from the NV center is detected. Simultaneously, microwave (MW) radiation is applied to the NV center. The MW frequency is scanned within a certain range containing the magnetic resonances. When the MW frequency is on resonance with one of the $m = 0 \leftrightarrow \pm 1$ transitions, the fluorescence level decreases since the MW field spoils the NV optical pumping, transferring NV centers to the $m = \pm 1$ sublevels which fluoresce less brightly. The associated spectrum showing the fluorescence intensity as a function of MW frequency is called an ODMR

Fig. 6 Sketch of an optically-detected magnetic resonance spectrum for a single NV center. The magnetic field is assumed to be along the NV axis



spectrum and is sketched in Fig. 6. In this drawing, we assume that the magnetic field is pointing along the NV axis. The magnetic field amplitude can be determined from the resonance frequencies. The fractional difference in fluorescence intensity between MW on- and off-resonance is called the fluorescence contrast \mathcal{C} . For single NV centers, a $\mathcal{C} = 0.20$ contrast is typical. Another important parameter is the linewidth of the magnetic resonance $\Delta\nu$. The linewidth is related to the inhomogeneously-broadened transverse spin relaxation time $T_2^* = 1/(\pi\Delta\nu)$, which is ≈ 100 ns for NV centers in HPHT diamond material rich in nitrogen [13] and a few μs for NV centers in diamonds with low nitrogen concentration. In order to measure the transition frequencies and thereby the magnetic field accurately, it is advantageous to have a large contrast and a narrow linewidth.

If instead of a single NV center, one has an ensemble of NV centers in the confocal volume, there may be in total eight magnetic resonances due to the four possible alignments of the NV center. For certain directions of the magnetic field, some resonances are degenerate. Figure 7 shows an example ODMR spectrum with a bias magnetic field along an arbitrary direction. One option for NV magnetometry is to select one NV alignment by applying a bias field along the NV axis so that changes in the magnetic field projection along this axis affect the resonance frequencies approximately linearly. Another option is to use all four NV alignments; although the eight ODMR frequencies have more complicated dependence on \mathbf{B} , this option yields vector information about the magnetic field.

7 DC Magnetometry

We will now discuss measurements of static or slowly-varying magnetic fields. To be more precise, with a dc magnetometer one can measure magnetic fields with frequency components from dc up to the bandwidth of the magnetometer (BW). The bandwidth can be measured by applying oscillating magnetic fields of increasing frequencies while recording the magnetometer response. The

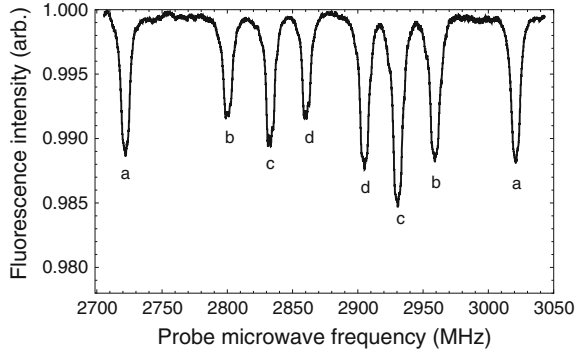


Fig. 7 An example ODMR plot with a magnetic field in an arbitrary direction. Each of the four NV alignments (labeled *a–d*) has a different magnetic field projection along its quantization axis, leading to eight ODMR peaks (two for each NV alignment). The ODMR frequencies are linear with \mathbf{B} when aligned along the NV axis. Although the ODMR frequencies have more complicated dependence when \mathbf{B} is along an arbitrary direction, we can extract the \mathbf{B} vector information by using multiple NV alignments. The asymmetry between the two peaks arising from the same alignment is due to differences in the applied microwave power

magnetometer signal decreases with increasing frequency, and the bandwidth is defined as the frequency where the signal has decreased by a factor of two. The signal-to-noise ratio (SNR) typically decreases with increasing frequency since the signal decreases. However, if the noise also decreases, it is possible to measure magnetic fields with frequencies above the BW with good SNR.

One way to measure the magnetic field is with CW ODMR. In this case, the MW frequency is scanned across the magnetic resonance within a certain time τ_{scan} . One can obtain a value for the magnetic field during each such time interval, and the bandwidth of the magnetometer will then be $\text{BW} \sim 1/\tau_{\text{scan}}$. Many microwave generators can only scan the frequency slowly ($\tau_{\text{scan}} \geq 10$ ms) such that the bandwidth will be small ($\text{BW} \leq 100$ Hz). The slow scan also makes the measurement sensitive to low-frequency technical noise or drifts in the experimental apparatus. Examples of noise sources include moving magnetic objects (cars, trains, elevators, and so on), 50/60 Hz magnetic fields from the line voltage, laser power fluctuations, fluctuations in the MW power or frequency, light polarization noise, temperature drifts, and so on. In order to make a sensitive measurement of the magnetic field, one can instead utilize a modulation technique. One possibility is to apply an oscillating magnetic field using an external coil and use lock-in detection [35]. Alternatively, one can modulate the microwave frequency [34, 37]. Many microwave generators have build-in frequency modulation (FM), making FM an easy approach to implement.

Consider the case depicted in Fig. 8 where the microwave frequency is modulated with the frequency f_{mod} around a central value f_c . The maximum excursion from the center frequency is called the frequency deviation f_{dev} . The center frequency should be chosen to be close to one of the magnetic resonance frequencies,

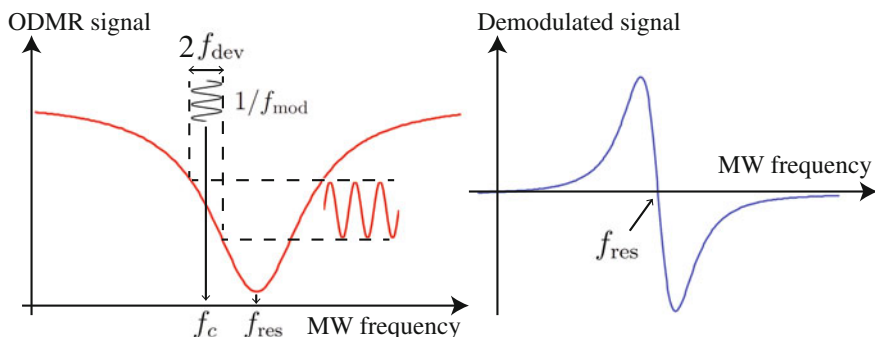


Fig. 8 *Left* Optically detected magnetic resonance signal. The MW frequency is modulated at the frequency f_{mod} around the central value f_c with a certain frequency deviation f_{dev} . *Right* The demodulated signal has a dispersive lineshape when sweeping the central frequency

here assumed to be the $m = 0 \rightarrow -1$ transition shown in Fig. 6. The detected fluorescence signal is then demodulated by a lock-in amplifier referenced to the modulation frequency. The demodulated signal S_{LI} has a dispersive lineshape with a zero crossing at $f_c = f_{\text{res}}$ and is linear $S_{\text{LI}} \approx \alpha(f_c - f_{\text{res}})$, where α is a proportionality constant, when $f_c - f_{\text{res}}$ is well within the linewidth of the magnetic resonance $\Delta\nu$. The demodulated signal can be used to measure slowly-varying magnetic fields $B(t) = B_0 + \Delta B(t)$, where B_0 is defined by the set value of the center frequency by the formula $f_c = D - \gamma B_0 / (2\pi)$. The demodulated signal is linear in the magnetic field deviation $\Delta B(t) = -2\pi S_{\text{LI}}(t) / (\alpha\gamma)$ and therefore provides a good measure for $\Delta B(t)$. The magnetometer bandwidth depends on the optical pump power and the microwave power, and for high powers a bandwidth as large as a few MHz has been demonstrated [40]. The maximum achievable bandwidth will in the end be limited by the lifetime of the metastable singlet state (≈ 200 ns at room temperature).

Methods from atomic clock technology can be used to make a pulsed NV magnetometer for dc magnetic fields (Fig. 9), a complementary technique to the CW methods described above. One way to implement this is to initialize the NV centers to the $m = 0$ sublevel, switch off the pump laser, apply a frequency-dependent microwave π -pulse to interrogate the $m = 0 \rightarrow +1$ or $m = 0 \rightarrow -1$ resonance frequency, and read out the final-state fluorescence with a second laser pulse. Similar to CW magnetometry, the microwave π -pulse duration

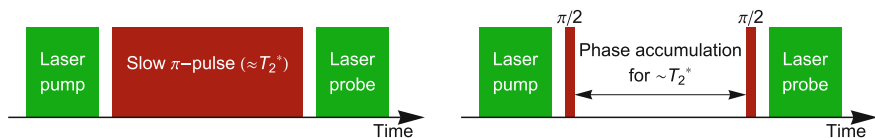


Fig. 9 Pulse sequences for ODMR experiments using a resonant π -pulse (*left*) or Ramsey spectroscopy (*right*)

τ_π and the inhomogeneously-broadened transverse spin relaxation time (T_2^*) contribute to the linewidth. A longer π -pulse has a narrower Fourier width, but excites fewer NV centers; choosing $\tau_\pi = T_2^*$ yields the best sensitivity [41]. Alternatively, one can measure the ODMR frequency with Ramsey interferometry, using two short $\pi/2$ -pulses separated by an interaction time ($\approx T_2^*$) to accumulate magnetic-field-dependent phase, which one can read out to extract the magnetic field.

8 AC Magnetometry

An ac magnetometer is sensitive to synchronized magnetic fields or asynchronized magnetic noise within a narrow bandwidth around a specific frequency. This is in contrast to a dc magnetometer which is sensitive to frequency components from dc up to the bandwidth of the sensor. ac magnetometry with NV centers is inspired by nuclear magnetic resonance (NMR) techniques where pulse sequences (called dynamical decoupling, or DD) of microwave or radio-frequency radiation are used to remove magnetic inhomogeneity and extend coherence lifetime (one example is Hahn echo). Decoupling sequences can extend the T_2^* coherence time to a considerably longer T_2 coherence time (2 ms at room temperature and 0.6 s at 77 K), though this is easiest to achieve in ^{13}C -depleted diamond samples with few defects [42, 43]. Though designed to remove ac and dc inhomogeneity in NMR, DD pulse sequences are sensitive to ac magnetic fields (and can act as band-pass filters or lock-in detectors). Decoupling sequences can be used to sense coherent ac fields and incoherent ac fields (magnetic noise) at kHz-MHz frequencies.

Figure 10 illustrates how a DD sequence (Hahn echo in this case) is useful for ac magnetometry. After initializing the NV centers to an equal superposition of two Zeeman sublevels with the first $\pi/2$ -pulse, the ac magnetic field (with frequency f_{AC} and period T_{AC}) with projection along the NV axis (B_{AC}) induces faster or slower Larmor precession, depending on its instantaneous sign. By choosing the pulse

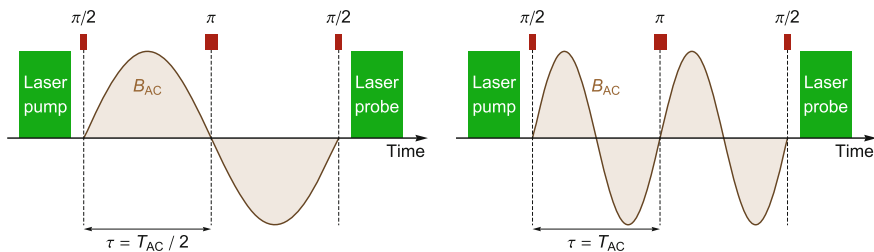


Fig. 10 *Left* The π -pulse allows us to keep the absolute value of the phase accumulation from B_{AC} . When sensing noise, this is how you get the most decoherence. *Right* Here, $\tau = T_{AC}$, and the phase accumulation cancels regardless of the relative phase and amplitude. This makes the NV centers immune to magnetic noise at f_{AC} , restoring coherence for this choice of τ (ESEEM)

spacing $\tau = T_{AC}/2$ and synchronizing the experiment and the ac magnetic field, one can maximize the phase accumulation the NV centers acquire from B_{AC} . Decoupling sequences also enable asynchronous ac magnetic noise detection. Choosing $\tau = T_{AC}/2$ also spoils the NV coherence if there is strong magnetic noise at f_{AC} , while choosing $\tau = T_{AC}$ makes the NV coherence immune to magnetic noise with frequency f_{AC} . This phenomenon is called electron spin echo envelope modulation (ESEEM) in electron paramagnetic resonance and is often used to sense and identify nearby magnetic nuclei [44]. Figure 11 shows some example measurements of ac magnetic noise detected with NV ensembles. The diamond samples contain a natural abundance of 1.1 % ^{13}C nuclear spins, which when located in a magnetic field will precess with the frequency of ≈ 10.705 MHz/T, leading to collapses and revivals in the NV coherence as the time τ is varied. The plot on the right includes data from an experiment with an externally-applied 707 kHz magnetic field from a function generator. The external field was not synchronized with the MW pulses and further spoiled the NV coherence for particular τ .

NV centers can also be used to sense incoherent nuclear and paramagnetic ac magnetic fields with other detection schemes. Correlation spectroscopy is a technique that extends DD sensing with some added benefits. It uses two DD sequences (separated by a time $\tilde{\tau}$) that each accumulate phase from an ac magnetic field [45]. This enables us to study the phase correlations in a nuclear spin bath with $\approx T_1^{-1}$ frequency resolution (instead of $\approx T_2^{-1}$ for DD). Another scheme is double electron-electron resonance (DEER), which can sense electronic spins using simultaneous NV and electronic π -pulses [28]. Similarly, one can detect NV decoherence when driving NV Rabi oscillations at a frequency that matches the desired ac frequency (a method called spin-locking) or driving both the NV centers and a target spin at the same Rabi frequency (called Hartmann-Hahn double resonance) [46, 47]. The resulting NV decoherence indicates the presence of an ac

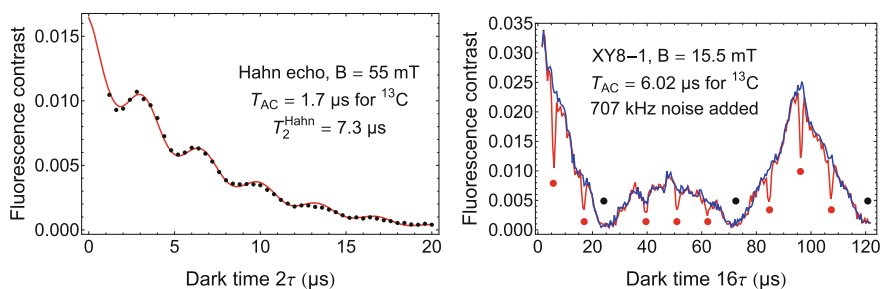


Fig. 11 *Left* Results of a Hahn echo experiment with an HPHT sample (~ 1 ppm NV^- concentration), showing the ESEEM coherence revivals caused by ^{13}C nuclei. *Right* Results of an XY8-1 experiment (another DD sequence with eight π -pulses) with a CVD sample (~ 10 ppb NV^- concentration). The *blue* data show how the NV coherence is most strongly spoiled by ^{13}C magnetic noise for dark times indicated by the *black circles*. The *red* data show the same experiment with an externally-applied (unsynchronized) 707 kHz magnetic field, which further spoils the coherence for dark times indicated by the *red circles*

magnetic field. One can also use NV T_1 measurements to detect paramagnetic spins or GHz-frequency magnetic white noise, as these sources spoil the NV T_1 lifetime [48–52].

9 Magnetic Field Sensitivity

The magnetic field sensitivity (in units of T/ $\sqrt{\text{Hz}}$) describes the smallest change in magnetic field one can detect with a measurement bandwidth of 1 Hz. For a given measurement time τ_m , the measurement bandwidth is approximately $1/(2\tau_m)$; the exact numerical factor depends on the details of the measurement. For simplicity, we assume here that the magnetometer has a 100 % duty cycle and that the sensitivity equals $\delta B\sqrt{\tau_m}$, where δB is the uncertainty on the measured magnetic field. Notice that if the measurement is repeated N times in a duration $T = N\tau_m$, the uncertainty will decrease by a factor of \sqrt{N} if the noise in the N measurements is uncorrelated. However, the sensitivity does not depend on the number of averages as the measurement time increases accordingly.

There are certain quantum limits to the sensitivity of an NV magnetometer. The most fundamental limit is due to the spin projection noise associated with the finite number of NV centers queried. The spin projection noise limited sensitivity is

$$\delta B_{\text{PN}}\sqrt{\tau_m} \approx \frac{1}{\gamma\sqrt{N_{\text{NV}}T_2}}, \quad (1)$$

where δB_{PN} is the magnetic field uncertainty due to the spin projection noise, γ is the electron gyromagnetic ratio, N_{NV} is the number of NV centers in the ensemble, and T_2 is the coherence time. The projection-noise limit can only be surpassed if one uses quantum entanglement of the sensing spins [53].

The photon shot noise of the light used to read out the NV spin state also limits the magnetic field sensitivity. This photon shot noise limited sensitivity is given by

$$\delta B_{\text{SN}}\sqrt{\tau_m} \approx \frac{\Delta\nu}{\gamma\mathcal{C}\sqrt{\mathcal{R}}}, \quad (2)$$

where δB_{SN} is the magnetic field uncertainty due to the photon shot noise, \mathcal{R} is the rate of detected photons, $\Delta\nu$ is the FWHM of the magnetic resonance, and \mathcal{C} is the contrast. The FWHM is related to the coherence time by the equation $T_2 = 1/(\pi\Delta\nu)$. The rate of detected photons can be calculated from the detected power $\mathcal{R} = P/(hc/\lambda)$, where P is the power, h is Planck's constant, c the speed of light, and λ is the wavelength of the detected light. Since the overall magnetometer signal S increases linearly with the rate of detected photons $S \propto \mathcal{R}$, and the uncertainty ΔS due to the photon shot noise increases only as the square-root $\Delta S \propto \sqrt{\mathcal{R}}$, the sensitivity improves as $\Delta S/S \propto \sqrt{\mathcal{R}}/\mathcal{R} = 1/\sqrt{\mathcal{R}}$.

The shot-noise-limited sensitivity and the projection-noise-limited sensitivity are in general different. However, under some conditions they can be of the same size. Consider an ensemble of NV centers continuously illuminated with pump light (as in a CW ODMR experiment). The excitation rate from the 3A_2 state to the 3E state is denoted Γ_P . The rate of emitted fluorescence is approximately $N_{\text{NV}}\Gamma_P$. The optimal excitation rate will be $\Gamma_P \approx 1/T_2$ as increasing the excitation rate beyond this will decrease the coherence time. Assuming that all the fluorescence is detected we find $\mathcal{R} \approx N_{\text{NV}}/T_2$. Finally assuming 100 % contrast we calculate $\delta B_{\text{SN}}\sqrt{\tau_m} \approx \delta B_{\text{PN}}\sqrt{\tau_m}$. We note that in most realistic situations both the light detection efficiency and the contrast are much smaller than 100 %, such that the shot noise limited sensitivity is worse than the projection noise limited sensitivity.

The parameters used to calculate spin projection noise and photon shot noise vary drastically depending on the experiment and diamond sample. The coherence time is generally longer for ac magnetometers compared to dc magnetometers, as the T_2 time obtained using Hahn echo or dynamical decoupling techniques can be much longer than the T_2^* time relevant for dc magnetometers. The coherence times T_2^* and T_2 also depend strongly on the diamond material and the particular DD sequence used. The rate of detected photons depends on the number of NV centers in the probed volume, the input pump power, and the light detection efficiency, which is typically quite low (a few percent) for a confocal setup. The number of NV centers used depends on the size of the probed volume and on the NV density, which depends on the diamond material and on the irradiation dose and annealing procedure. Finally, the fluorescence contrast can be up to 20 % for a single NV center, while for ensembles of NV centers the contrast is typically much smaller due to background fluorescence.

There are several ways to assess magnetometer sensitivity experimentally. With a CW magnetometer, one can apply a constant field, measure this field continuously, and calculate the noise floor after taking the Fourier transform. With a pulsed magnetometer that reports discrete values, one can apply a constant field and calculate the standard deviation of the resulting magnetic field values (normalizing to 1 Hz bandwidth). A similar approach is to apply slightly different fields and determine how long it takes to distinguish them.

The highest sensitivities which have been demonstrated with an NV ensemble are 15 pT/ $\sqrt{\text{Hz}}$ (dc sensing) and 1 pT/ $\sqrt{\text{Hz}}$ (ac sensing) [54, 55]. The magnetometer sensitivity in Ref. [54] is nearly photon shot noise limited, though the spin projection noise is ~ 10 fT/ $\sqrt{\text{Hz}}$. There has been rapid progress in recent years on improving the magnetic field sensitivity of NV magnetometers, and with additional improvements sub-pT/ $\sqrt{\text{Hz}}$ sensitivity will soon be achievable.

10 Applications

NV magnetometers are most appropriate for sensing applications requiring high spatial resolution, especially those where it is possible to put the NV centers close to the system being measured. As described above, NV centers can sense paramagnetic and nuclear spins a few nanometers away using T_1 and T_2 ac magnetometry schemes. NV T_1 relaxation is better suited for sensing GHz-frequency magnetic noise, which lends itself well to sensing paramagnetic spins and magnetic Johnson noise [48–52]. Since nuclei have 0.1–1 MHz Larmor precession at a few tens of millitesla, T_2 relaxation is useful for sensing magnetic nuclei (such as ^1H , ^{13}C , ^{19}F , ^{29}Si , and ^{31}P) [44, 56, 57, 58]. One eventual goal is to achieve single-molecule MRI, where an NV center can sense nearby magnetic nuclei and distinguish their positions, allowing us to reconstruct the structure of complex molecules such as proteins.

While many NV experiments seek new magnetic sensitivity limits or study a well-understood target system, the most exciting projects are those that use NV sensing in a new context. NV wide-field magnetic imaging examined 50 nm ferromagnetic grains in magnetotactic bacteria, 10–100 μm grains in meteorites, and immunomagnetically-labeled cancer cells [59–61]. Due to the high spatial resolution and non-toxicity of diamond, NV applications extend to neuroscience and biology. One experiment measured the magnetic field in a living cell to probe intracellular dynamics with nanodiamonds [17]. In neuroscience, NV magnetometers aim to sense the magnetic field from a firing neuron and study how neural networks form connections as they grow on a diamond [26, 54]. Soon NV magnetometry will enable NMR and MRI for molecules near the diamond surface. NV magnetometers have sensed the stray fields from magnetic domains in hard disk drives and show potential for characterizing read/write heads [15].

Finally, NV magnetometers are a promising tool for investigating magnetic phenomena in condensed-matter physics, such as the Meissner effect and magnetic flux vortices in superconductors [62]. NV AFM experiments have also examined domain walls and vortices in magnetic thin films [63, 64]. Another experiment used individual NV centers to study magnetic spin-wave excitations in a ferromagnetic microdisk [65]. NV magnetometers also show potential for investigating skyrmion, spin ice, and other exotic materials [3, 66]. Finally, NV decoherence measurements reveal information about the magnetic spin bath dynamics (for both nuclear and paramagnetic spins).

11 Advantages and Ongoing Challenges

As sensors, NV centers have unprecedented spatial resolution. The NV electronic wave function is constrained to a few atomic lattice sites (~ 0.5 nm) and the spatial resolution can be hundreds of nanometers when using diffraction-limited optics,

while optical superresolution techniques can do even better. An NV ensemble provides vector information about the magnetic field (instead of a projection). Furthermore, NV centers can work as simultaneous magnetic field, electric field, temperature, compression, and rotation sensors in the same device [67–72].

Another advantage is the technical simplicity of NV magnetometers. Often the pump laser is a common frequency-doubled 532 nm Nd:YAG laser, and high polarization and frequency stability are usually unnecessary (in contrast to other optical magnetometers). Furthermore, NV centers are easy to optically initialize and read out compared to other atomic physics systems. Other magnetic sensing technologies require specific environments (near-zero magnetic field, cryogenics, or ultra-high vacuum). Isolating the sensor in a cryogenic or vacuum environment separates it from the system being sensed, and with the additional distance comes reduced spatial resolution and reduced magnetic field from external sources. NV sensors are versatile and robust, allowing us to compensate for the lower magnetic field sensitivity by placing the NV centers a few nanometers away from the target, where the field is stronger. Most NV experiments are done in ambient conditions, though they also work at extreme pressures and temperatures [68, 73].

Many of these advantages come from the diamond material properties themselves. Diamond is chemically inert and biocompatible; living cells can rest on top of a diamond substrate and can uptake nanodiamonds without being poisoned. NV centers have long relaxation times at room temperature because of the strong carbon-carbon bonds in diamond, leading to a high Debye temperature (~ 2200 K [14]). With improvements in fabrication and implantation technology, one will be able to deterministically place NV centers in a diamond sample and fabricate diamond nanostructures (including diamond nanopillars) for increased light collection efficiency and for magnetometry with high spatial resolution.

Despite their advantages, NV centers have many technical challenges to overcome. Diamond has a high refractive index, so most of the fluorescence light emitted from an NV in a flat diamond is not collected in a confocal microscope. This means that despite the small spin-projection noise, NV experiments are instead limited by photon shot noise (or other noise sources), which is often many orders of magnitude larger. Inhomogeneous broadening is another problem; local magnetic fields and crystal strains broaden the ODMR resonances, reduce T_2^* , and diminish sensitivity. Using high-density samples with many NV centers may improve ensemble sensitivity, but this comes at the cost of more broadening from radiation damage, nitrogen defects, and crystal strain. Sample-dependent results also complicates development—diamond samples differ in crystal growth conditions, surface treatment, irradiation, NV depth, and impurity content. This makes some goals achievable only with certain samples, and one must study how to reproducibly produce desirable samples.

Compared to the atoms used in other optical magnetometers (Rb, Cs, He, and so on), which have well-understood basic properties (such as electronic configurations, transition frequencies, and electric dipole moments), NV centers are still not fully understood. The ${}^3A_2 \leftrightarrow {}^3E$ and ${}^1E \leftrightarrow {}^1A_1$ energies are known (Fig. 2), but the

relative triplet-singlet energies and their energies compared to the diamond valence and conduction bands are not known directly [74–76]. Similarly, the optical pumping mechanism, which all NV experiments take advantage of for initialization and readout, is not completely understood. Furthermore, although four of the six anticipated electronic states are experimentally confirmed, the remaining two have yet to be found.

NV magnetometers have some inconvenient limitations. Transverse crystal strain (which can be up to ~ 10 MHz) makes low-field magnetometry challenging. NV centers are also simultaneously a magnetometer and a thermometer, meaning uncompensated temperature drifts can be interpreted as changes in magnetic field. Querying both of the $m = 0 \leftrightarrow \pm 1$ transitions can mitigate this problem and cancel temperature drifts [77, 78]. Finally, although near-surface NV centers are best for sensing external magnetic fields, their properties (photostability and coherence time) deteriorate at shallower depths because of magnetic noise from unbonded electrons at the diamond surface [20].

12 Summary

It has only been a few years since NV-based sensors burst into the field of optical magnetometry, promising to revolutionize it with an unprecedented combination of high sensitivity and spatial resolution. While the technical challenges facing diamond sensors are substantial, the promise has already been fulfilled, largely through a plethora of novel applications that have become possible due to the unique properties of NV sensors. With the ongoing advances and ever-growing breadth of utility, we are sure this is only the beginning.

Acknowledgements We thank Victor Acosta, Yannick Dumeige, Dmitry Farfurnik, Andrey Jarmola, and Nathan Leefer for insightful discussions and comments on the manuscript. Our research was supported in part by German-Israeli Project Cooperation (DIP) program, the NSF through grant No. ECCS-1202258, and the AFOSR/DARPA QuASAR program. K. J. acknowledges support from the Carlsberg Foundation.

References

1. R. Schirhagl, K. Chang, M. Loretz, C.L. Degen, Nitrogen-vacancy centers in diamond: nanoscale sensors for physics and biology. *Annu. Rev. Phys. Chem.* **65**(1), 83 (2014)
2. M.W. Doherty, N.B. Manson, P. Delaney, F. Jelezko, J. Wrachtrup, L.C.L. Hollenberg, The nitrogen-vacancy colour centre in diamond. *Phys. Rep.* **528**(1), 1 (2013)
3. L. Rondin, J.-P. Tetienne, T. Hingant, J.-F. Roch, P. Maletinsky, V. Jacques, Magnetometry with nitrogen-vacancy defects in diamond. *Rep. Prog. Phys.* **77**(5), 056503 (2014)
4. V.M. Acosta, D. Budker, P.R. Hemmer, J.R. Maze, R.L. Walsworth, Optical magnetometry with nitrogen-vacancy centers in diamond, in *Optical Magnetometry*, ed. by D. Budker, D.F. Jackson Kimball (Cambridge University Press, Cambridge, 2013), pp. 142–166

5. J.R. Maze, A. Gali, E. Togan, Y. Chu, A. Trifonov, E. Kaxiras, M.D. Lukin, Properties of nitrogen-vacancy centers in diamond: the group theoretic approach. *New J. Phys.* **13**(2), 025025 (2011)
6. M.W. Doherty, N.B. Manson, P. Delaney, L.C.L. Hollenberg, The negatively charged nitrogen-vacancy centre in diamond: the electronic solution. *New J. Phys.* **13**, 025019 (2011)
7. L. Robledo, H. Bernien, T. van der Sar, R. Hanson, Spin dynamics in the optical cycle of single nitrogen-vacancy centres in diamond. *New J. Phys.* **13**, 025013 (2011)
8. J.-P. Tetienne, L. Rondin, P. Spinicelli, M. Chipaux, T. Debuisschert, J.-F. Roch, V. Jacques, Magnetic-field-dependent photodynamics of single NV defects in diamond: an application to qualitative all-optical magnetic imaging. *New J. Phys.* **14**, 103033 (2012)
9. V.M. Acosta, A. Jarmola, E. Bauch, D. Budker, Optical properties of the nitrogen-vacancy singlet levels in diamond. *Phys. Rev. B* **82**, 201202 (2010)
10. S. Felton, A.M. Edmonds, M.E. Newton, P.M. Martineau, D. Fisher, D.J. Twitchen, J.M. Baker, Hyperfine interaction in the ground state of the negatively charged nitrogen vacancy center in diamond. *Phys. Rev. B* **79**, 075203 (2009)
11. B. Smeltzer, J. McIntyre, L. Childress, Robust control of individual nuclear spins in diamond. *Phys. Rev. A* **80**, 050302 (2009)
12. M. Steiner, P. Neumann, J. Beck, F. Jelezko, J. Wrachtrup, Universal enhancement of the optical readout fidelity of single electron spins at nitrogen-vacancy centers in diamond. *Phys. Rev. B* **81**, 035205 (2010)
13. V.M. Acosta, E. Bauch, M.P. Ledbetter, C. Santori, K.-M.C. Fu, P.E. Barclay, R.G. Beausoleil, H. Linget, J.F. Roch, F. Treussart, S. Chemerisov, W. Gawlik, D. Budker, Diamonds with a high density of nitrogen-vacancy centers for magnetometry applications. *Phys. Rev. B* **80**, 115202 (2009)
14. A.M. Zaitsev, *Optical Properties of Diamond: A Data Handbook* (Springer, New York, 2001)
15. P. Maletinsky, S. Hong, M.S. Grinolds, B. Hausmann, M.D. Lukin, R.L. Walsworth, M. Loncar, A. Yacoby, A robust scanning diamond sensor for nanoscale imaging with single nitrogen-vacancy centres. *Nat. Nanotechnol.* **7**, 320 (2012)
16. M. Geiselmann, M.L. Juan, J. Renger, J.M. Say, L.J. Brown, F.J.G. de Abajo, F. Koppens, R. Quidant, Three-dimensional optical manipulation of a single electron spin. *Nat. Nanotechnol.* **8**, 175 (2013)
17. L.P. McGuinness, Y. Yan, A. Stacey, D.A. Simpson, L.T. Hall, D. Maclaurin, S. Praver, P. Mulvaney, J. Wrachtrup, F. Caruso, R.E. Scholten, L.C.L. Hollenberg, Quantum measurement and orientation tracking of fluorescent nanodiamonds inside living cells. *Nat. Nanotechnol.* **6**, 358 (2011)
18. M. Lesik, J.-P. Tetienne, A. Tallaire, J. Achard, V. Mille, A. Gicquel, J.-F. Roch, V. Jacques, Perfect preferential orientation of nitrogen-vacancy defects in a synthetic diamond sample. *Appl. Phys. Lett.* **104**(11), 113107 (2014)
19. K. Ohno, F.J. Heremans, L.C. Bassett, B.A. Myers, D.M. Toyli, A.C.B. Jayich, C. J. Palmstrom, D.D. Awschalom, Engineering shallow spins in diamond with nitrogen delta-doping. *Appl. Phys. Lett.* **101**(8), 082413 (2012)
20. B.A. Myers, A. Das, M.C. Dartiailh, K. Ohno, D.D. Awschalom, A.C. Bleszynski, Jayich. Probing Surface Noise with Depth-Calibrated Spins in Diamond. *Phys. Rev. Lett.* **113**, 027602 (2014)
21. L.-J. Su, C.-Y. Fang, Y.-T. Chang, K.-M. Chen, Y.-C. Yu, J.-H. Hsu, H.-C. Chang, Creation of high density ensembles of nitrogen-vacancy centers in nitrogen-rich type Ib nanodiamonds. *Nanotechnology* **24**(31), 315702 (2013)
22. P. Andrich, B.J. Aleman, J.C. Lee, K. Ohno, C.F. de las Casas, F.J. Heremans, E.L. Hu, D.D. Awschalom, Engineered micro- and nanoscale diamonds as mobile probes for high-resolution sensing in fluid. *Nano Lett.* **14**(9), 4959 (2014)
23. B.J.M. Hausmann, T.M. Babinec, J.T. Choy, J.S. Hodges, S. Hong, I. Bulu, A. Yacoby, M.D. Lukin, M. Loncar, Single-color centers implanted in diamond nanostructures. *New J. Phys.* **13**(4), 045004 (2011)

24. M.J. Burek, Y. Chu, M.S. Z. Liddy, P. Patel, J. Rochman, S. Meesala, W. Hong, Q. Quan, M. D. Lukin, M. Loncar, High quality-factor optical nanocavities in bulk single-crystal diamond. *Nat. Commun.* **5** (2014)
25. J.R. Maze, P.L. Stanwix, J.S. Hodges, S. Hong, J.M. Taylor, P. Cappellaro, L. Jiang, M.V. Gurudev Dutt, E. Togan, A.S. Zibrov, A. Yacoby, R.L. Walsworth, M.D. Lukin, Nanoscale magnetic sensing with an individual electronic spin in diamond. *Nature* **455**, 644 (2008)
26. L.M. Pham, D. Le Sage, P.L. Stanwix, T.K. Yeung, D. Glenn, A. Trifonov, P. Cappellaro, P. R. Hemmer, M.D. Lukin, H. Park, A. Yacoby, R.L. Walsworth, Magnetic field imaging with nitrogen-vacancy ensembles. *New J. Phys.* **13**(4), 045021 (2011)
27. D. Wildanger, B.R. Patton, H. Schill, L. Marseglia, J.P. Hadden, S. Knauer, A. Schönle, J.G. Rarity, J.L. O'Brien, S.W. Hell, J.M. Smith, Solid immersion facilitates fluorescence microscopy with nanometer resolution and sub-angstrom emitter localization. *Adv. Mater.* **24** (44), OP309 (2012)
28. M.S. Grinolds, M. Warner, K. De Greve, Y. Dovzhenko, L. Thiel, R.L. Walsworth, S. Hong, P. Maletinsky, A. Yacoby, Subnanometre resolution in three-dimensional magnetic resonance imaging of individual dark spins. *Nat. Nanotechnol.* **9**, 279 (2014)
29. D. Le Sage, L.M. Pham, N. Bar-Gill, C. Belthangady, M.D. Lukin, A. Yacoby, R.L. Walsworth, Efficient photon detection from color centers in a diamond optical waveguide. *Phys. Rev. B* **85**, 121202 (2012)
30. B.J. Shields, Q.P. Unterreithmeier, N.P. de Leon, H. Park, M.D. Lukin, Efficient readout of a single spin state in diamond via spin-to-charge conversion. *Phys. Rev. Lett.* **114**, 136402 (2015)
31. L. Robledo, L. Childress, H. Bernien, B. Hensen, P.F.A. Alkemade, R. Hanson, High-fidelity projective read-out of a solid-state spin quantum register. *Nature* **477**, 574 (2011)
32. P. Siyushev, F. Kaiser, V. Jacques, I. Gerhardt, S. Bischof, H. Fedder, J. Dodson, M. Markham, D. Twitchen, F. Jelezko, J. Wrachtrup, Monolithic diamond optics for single photon detection. *Appl. Phys. Lett.* **97**, 241902 (2010)
33. J.P. Hadden, J.P. Harrison, A.C. Stanley-Clarke, L. Marseglia, Y.-L.D. Ho, B.R. Patton, J.L. O'Brien, J.G. Rarity, Strongly enhanced photon collection from diamond defect centers under microfabricated integrated solid immersion lenses. *Appl. Phys. Lett.* **97**, 241901 (2010)
34. V.M. Acosta, K. Jensen, C. Santori, D. Budker, R.G. Beausoleil, Electromagnetically induced transparency in a diamond spin ensemble enables all-optical electromagnetic field sensing. *Phys. Rev. Lett.* **110**, 213605 (2013)
35. V.M. Acosta, E. Bauch, A. Jarmola, L.J. Zipp, M.P. Ledbetter, D. Budker, Broadband magnetometry by infrared-absorption detection of nitrogen-vacancy ensembles in diamond. *Appl. Phys. Lett.* **97**, 174104 (2010)
36. Y. Dumeige, M. Chipaux, V. Jacques, F. Treussart, J.-F. Roch, T. Debuisschert, V. Acosta, A. Jarmola, K. Jensen, P. Kehayias, D. Budker, Magnetometry with nitrogen-vacancy ensembles in diamond based on infrared absorption in a doubly resonant optical cavity. *Phys. Rev. B* **87**, 155202 (2013)
37. K. Jensen, N. Leefer, A. Jarmola, Y. Dumeige, M. Acosta, V.P. Kehayias, B. Patton, D. Budker, Cavity-enhanced room-temperature magnetometry using absorption by nitrogen-vacancy centers in diamond. *Phys. Rev. Lett.* **112**, 160802 (2014)
38. P. Kehayias, M.W. Doherty, D. English, R. Fischer, A. Jarmola, K. Jensen, N. Leefer, P. Hemmer, N.B. Manson, D. Budker, Infrared absorption band and vibronic structure of the nitrogen-vacancy center in diamond. *Phys. Rev. B* **88**, 165202 (2013)
39. E. Bourgeois, A. Jarmola, P. Siyushev, M. Gulka, J. Hruby, F. Jelezko, D. Budker, M. Nesladek, Photoelectric detection of electron spin resonance of nitrogen-vacancy centres in diamond. *Nat. Commun.* **6**, 8577 (2015)
40. C.S. Shin, C.E. Avalos, M.C. Butler, D.R. Trease, S.J. Seltzer, J.P. Mustonen, D.J. Kennedy, V.M. Acosta, D. Budker, A. Pines, V.S. Bajaj, Room-temperature operation of a radiofrequency diamond magnetometer near the shot-noise limit. *J. Appl. Phys.* **112**(12), 124519 (2012)

41. A. Dréau, M. Lesik, L. Rondin, P. Spinicelli, O. Arcizet, J.-F. Roch, V. Jacques, Avoiding power broadening in optically detected magnetic resonance of single NV defects for enhanced dc magnetic field sensitivity. *Phys. Rev. B* **84**, 195204 (2011)
42. L.M. Pham, N. Bar-Gill, C. Belthangady, D. Le Sage, P. Cappellaro, M.D. Lukin, A. Yacoby, R.L. Walsworth, Enhanced solid-state multispin metrology using dynamical decoupling. *Phys. Rev. B* **86**, 045214 (2012)
43. N. Bar-Gill, L.M. Pham, A. Jarmola, D. Budker, R.L. Walsworth, Solid-state electronic spin coherence time approaching one second. *Nat. Commun.* **4**, 1743 (2012)
44. S.J. DeVience, L.M. Pham, I. Lovchinsky, A.O. Sushkov, N. Bar-Gill, C. Belthangady, F. Casola, M. Corbett, H. Zhang, M. Lukin, H. Park, A. Yacoby, R.L. Walsworth, Nanoscale NMR spectroscopy and imaging of multiple nuclear species. *Nat. Nanotechnol.* **10**, 129 (2015)
45. A. Laraoui, F. Dolde, C. Burk, F. Reinhard, J. Wrachtrup, C.A. Meriles, High-resolution correlation spectroscopy of ^{13}C spins near a nitrogen-vacancy centre in diamond. *Nat. Commun.* **4**, 1651 (2013)
46. C. Belthangady, N. Bar-Gill, L.M. Pham, K. Arai, D. Le Sage, P. Cappellaro, R.L. Walsworth, Dressed-state resonant coupling between bright and dark spins in diamond. *Phys. Rev. Lett.* **110**, 157601 (2013)
47. P. London, J. Scheuer, J.-M. Cai, I. Schwarz, A. Retzker, M.B. Plenio, M. Katagiri, T. Teraji, S. Koizumi, J. Isoya, R. Fischer, L.P. McGuinness, B. Naydenov, F. Jelezko, Detecting and polarizing nuclear spins with double resonance on a single electron spin. *Phys. Rev. Lett.* **111**, 067601 (2013)
48. A. Jarmola, V.M. Acosta, K. Jensen, S. Chemerisov, D. Budker, Temperature- and magnetic-field-dependent longitudinal spin relaxation in nitrogen-vacancy ensembles in diamond. *Phys. Rev. Lett.* **108**, 197601 (2012)
49. S. Steinert, F. Ziem, L.T. Hall, A. Zappe, M. Schweikert, N. Götz, A. Aird, G. Balasubramanian, L. Hollenberg, J. Wrachtrup, Magnetic spin imaging under ambient conditions with sub-cellular resolution. *Nat. Commun.* **4** (2013)
50. A.O. Sushkov, N. Chisholm, I. Lovchinsky, M. Kubo, P.K. Lo, S.D. Bennett, D. Hunger, A. Akimov, R.L. Walsworth, H. Park, M.D. Lukin, All-optical sensing of a single-molecule electron spin. *Nano Lett.* **14**(11), 6443 (2014)
51. S. Kolkowitz, A. Safira, A.A. High, R.C. Devlin, S. Choi, Q.P. Unterreithmeier, D. Patterson, A.S. Zibrov, V.E. Manucharyan, H. Park, M.D. Lukin, Probing Johnson noise and ballistic transport in normal metals with a single-spin qubit. *Science* **347**(6226), 1129 (2015)
52. L.T. Hall, P. Kehayias, D.A. Simpson, A. Jarmola, A. Stacey, D. Budker, L.C.L. Hollenberg, Detection of nanoscale electron spin resonance spectra demonstrated using nitrogen-vacancy centre probes in diamond. *Nat. Commun.* **7**, 10211 (2016)
53. W. Wasilewski, K. Jensen, H. Krauter, J.J. Renema, M.V. Balabas, E.S. Polzik, Quantum noise limited and entanglement-assisted magnetometry. *Phys. Rev. Lett.* **104**, 133601 (2010)
54. J.F. Barry, M.J. Turner, J.M. Schloss, D.R. Glenn, Y. Song, M.D. Lukin, H. Park, R.L. Walsworth, Optical magnetic detection of single-neuron action potentials using quantum defects in diamond. [arXiv:1602.01056](https://arxiv.org/abs/1602.01056) (2016)
55. T. Wolf, P. Neumann, K. Nakamura, H. Sumiya, T. Ohshima, J. Isoya, J. Wrachtrup, Subpicotesla diamond magnetometry. *Phys. Rev. X* **5**, 041001 (2015)
56. H.J. Mamin, M. Kim, M.H. Sherwood, C.T. Rettner, K. Ohno, D.D. Awschalom, D. Rugar, Nanoscale nuclear magnetic resonance with a nitrogen-vacancy spin sensor. *Science* **339**(6119), 557 (2013)
57. T. Staudacher, F. Shi, S. Pezzagna, J. Meijer, J. Du, C.A. Meriles, F. Reinhard, J. Wrachtrup, nuclear magnetic resonance spectroscopy on a (5-Nanometer)³ sample volume. *Science* **339**(6119), 561 (2013)
58. C. Müller, X. Kong, J.-M. Cai, K. Melentjević, A. Stacey, M. Markham, D. Twitchen, J. Isoya, S. Pezzagna, J. Meijer, J.F. Du, M.B. Plenio, B. Naydenov, L.P. McGuinness, F. Jelezko, Nuclear magnetic resonance spectroscopy with single spin sensitivity. *Nat. Commun.* **5**(4703) (2014)

59. D. Le Sage, K. Arai, D.R. Glenn, S.J. DeVience, L.M. Pham, L. Rahn-Lee, M.D. Lukin, A. Yacoby, A. Komeili, R.L. Walsworth, Optical magnetic imaging of living cells. *Nature* **496**, 486 (2013)
60. R.R. Fu, B.P. Weiss, E.A. Lima, R.J. Harrison, X.-N. Bai, S.J. Desch, D.S. Ebel, C. Suavet, H. Wang, D. Glenn, D. Le Sage, T. Kasama, R.L. Walsworth, A.T. Kuan, Solar nebula magnetic fields recorded in the Semarkona meteorite. *Science* **346**(6213), 1089 (2014)
61. D.R. Glenn, K. Lee, H. Park, R. Weissleder, A. Yacoby, M.D. Lukin, H. Lee, R.L. Walsworth, C.B. Connolly, Single-cell magnetic imaging using a quantum diamond microscope. *Nat. Methods* (2015)
62. A. Waxman, Y. Schlüssel, D. Groswasser, V.M. Acosta, L.-S. Bouchard, D. Budker, R. Folman, Diamond magnetometry of superconducting thin films. *Phys. Rev. B* **89**, 054509 (2014)
63. J.-P. Tetienne, T. Hingant, J.-V. Kim, L. Herrera Diez, J.-P. Adam, K. Garcia, J.-F. Roch, S. Rohart, A. Thiaville, D. Ravelosona, V. Jacques, Nanoscale imaging and control of domain-wall hopping with a nitrogen-vacancy center microscope. *Science* **344**(6190), 1366 (2014)
64. L. Rondin, J.-P. Tetienne, S. Rohart, A. Thiaville, T. Hingant, P. Spinicelli, J.-F. Roch, V. Jacques, Stray-field imaging of magnetic vortices with a single diamond spin. *Nat. Commun.* **4**, 2279 (2013)
65. T. van der Sar, F. Casola, R. Walsworth, A. Yacoby, Nanometre-scale probing of spin waves using single electron spins. *Nat. Commun.* **6**, 7886 (2015)
66. A. Dussaux, P. Schoenherr, K. Chang, N. Kanazawa, Y. Tokura, C.L. Degen, D. Meier, Observation of local magnetization dynamics in the helimagnet FeGe. [arXiv:1503.06622](https://arxiv.org/abs/1503.06622) (2015)
67. F. Dolde, H. Fedder, M.W. Doherty, T. Nöbauer, F. Rempp, G. Balasubramanian, T. Wolf, F. Reinhard, L.C.L. Hollenberg, F. Jelezko, J. Wrachtrup, Electric-field sensing using single diamond spins. *Nat. Phys.* **7**, 459 (2011)
68. M.W. Doherty, V.V. Struzhkin, D.A. Simpson, L.P. McGuinness, Y. Meng, A. Stacey, T. J. Karle, R.J. Hemley, N.B. Manson, L.C.L. Hollenberg, S. Prawer, Electronic properties and metrology applications of the diamond NV center under pressure. *Phys. Rev. Lett.* **112**, 047601 (2014)
69. V.M. Acosta, E. Bauch, M.P. Ledbetter, A. Waxman, L.-S. Bouchard, D. Budker, Temperature dependence of the nitrogen-vacancy magnetic resonance in diamond. *Phys. Rev. Lett.* **104**, 070801 (2010)
70. D. Maclaurin, M.W. Doherty, L.C.L. Hollenberg, A.M. Martin, Measurable quantum geometric phase from a rotating single spin. *Phys. Rev. Lett.* **108**, 240403 (2012)
71. M.P. Ledbetter, K. Jensen, R. Fischer, A. Jarmola, D. Budker, Gyroscopes based on nitrogen-vacancy centers in diamond. *Phys. Rev. A* **86**, 052116 (2012)
72. A. Ajoy, P. Cappellaro, Stable three-axis nuclear-spin gyroscope in diamond. *Phys. Rev. A* **86**, 062104 (2012)
73. D.M. Toyli, C.F. de las Casas, D.J. Christle, V.V. Dobrovitski, D.D. Awschalom, Fluorescence thermometry enhanced by the quantum coherence of single spins in diamond. *Proc. Natl. Acad. Sci.* **110**(21), 8417 (2013)
74. N. Aslam, G. Waldherr, P. Neumann, F. Jelezko, J. Wrachtrup, Photo-induced ionization dynamics of the nitrogen vacancy defect in diamond investigated by single-shot charge state detection. *New J. Phys.* **15**(1), 013064 (2013)
75. D.M. Toyli, D.J. Christle, A. Alkauskas, B.B. Buckley, C.G. Van de Walle, D.D. Awschalom, Measurement and control of single nitrogen-vacancy center spins above 600 K. *Phys. Rev. X* **2**, 031001 (2012)
76. M.L. Goldman, M.W. Doherty, A. Sipahigil, N.Y. Yao, S.D. Bennett, N.B. Manson, A. Kubanek, M.D. Lukin, State-selective intersystem crossing in nitrogen-vacancy centers. *Phys. Rev. B* **91**, 165201 (2015)

77. K. Fang, V.M. Acosta, C. Santori, Z. Huang, K.M. Itoh, H. Watanabe, S. Shikata, R.G. Beausoleil, High-sensitivity magnetometry based on quantum beats in diamond nitrogen-vacancy centers. *Phys. Rev. Lett.* **110**, 130802 (2013)
78. H.J. Mamin, M.H. Sherwood, M. Kim, C.T. Rettner, K. Ohnoand, D.D. Awschalom, D. Rugar, Multipulse double-quantum magnetometry with near-surface nitrogen-vacancy centers. *Phys. Rev. Lett.* **113**, 030803 (2014)